RESEARCH ARTICLE

NANO · MICRO small
www.small-journal.com

Electromechanical Energy Conversion in Bouncing Ball Triboelectric Nanogenerator

Fangyang Dong, Guang-An Yu, Zhiying Zhang, Zhixiang Chen, Hengxu Du, Qiang Zhao, Taili Du, Tongming Zhou,* and Minyi Xu**

Understanding the dynamic behaviors and electromechanical conversion characteristics of triboelectric nanogenerators (TENGs) is essential for their precise design and optimization, yet these processes remain insufficiently elucidated. This study systematically investigates a bouncing ball TENG to clarify the coupled mechanical-electrical mechanisms through dynamic simulations and experimental validation. The dynamic behaviors of the bouncing ball under varying vibration conditions are analyzed, revealing four typical motion states directly associated with energy generation. Key parameters affecting these behaviors are identified, providing practical guidance for structural design and performance enhancement. Furthermore, a dual-simulation coupling method integrating dynamic modeling and finite element analysis is proposed, enabling accurate prediction of electric potentials and output waveforms without extensive experimental repetition. The results establish a unified framework for understanding and predicting TENG performance, contributing to the standardization and practical deployment of triboelectric energy harvesting technologies.

1. Introduction

Energy harvesting technology enables the development of sustainable and self-powered systems capable of supplying in situ power to wireless sensor nodes in the Internet of Things applications.[1,2] To extract useful electricity from ambient energy sources, research has increasingly focused on scavenging solar,[3] heat,[4] wind,[5] wave,[6] vibration[7,8] and human motion[9] energy. Among these, widely distributed mechanical vibration is particularly attractive due to its considerable power density (typically about ≈10–300 mW cm^{-3}[10]), which matches the required power level of the MEMS-based sensors.[11] This makes vibration-generated electricity an ideal candidate for powering numerous distributed nodes, especially in indoor environments where solar and wind energy are unavailable, such as on ships,[12,13] in factories,[14] buildings[15,16] or even within living bodies.[17] Various energy harvesters based on piezoelectric,[18] electromagnetic[19] and triboelectric[7] effects have been developed to convert mechanical vibration into electrical energy. Relevant beneficial research strives to leverage the advantages of these technologies, of which, triboelectric energy harvesting is highly adaptable for a broad vibration frequency range, from below 1 Hz to several hundred Hz.[7,20] Furthermore, for occasions with compact layouts, triboelectric technology offers an additional advantage for its compatibility with MEMS integration,[2] making it well-suited for powering distributed nodes.

In recent years, numerous innovative studies on vibration harvesters and sensors based on triboelectric nanogenerator (TENG) have been conducted, mainly in two optimal operating modes: contact-separation (C-S) and freestanding-layer modes.[7] The C-S mode, while capable of harvesting energy efficiently at resonance through vertical reciprocation, suffers from severe performance degradation outside its resonant frequency, limiting its broadband applicability. In contrast, the freestanding-layer mode provides higher mechanical adaptability, allowing for diverse motion types without relying on elastic restoring structures such as springs or cantilevers. Among various freestanding designs, the bouncing ball configuration has emerged as one of the simplest yet most robust architectures,[7] as shown in **Figure 1a**. In this configuration, a ball serves as the freestanding layer, repeatedly bouncing or rolling on other triboelectric materials or electrodes under external vibration, generating electricity through successive contact-separation cycles (Figure 1b). The nonlinear stiffness of the hard ball enables the bouncing ball TENG (BB-TENG) to

F. Dong, G.-A. Yu, Z. Zhang, H. Du, T. Du, M. Xu
Dalian Key Lab of Marine Micro/Nano Energy and Self-Powered Systems
Marine Engineering College
Dalian Maritime University
Dalian 116026, China
E-mail: dutaili@dlmu.edu.cn; xuminyi@dlmu.edu.cn

Z. Chen, T. Du
Collaborative Innovation Research Institute of Autonomous Ship
Dalian Maritime University
Dalian 116026, China

Q. Zhao
College of Mechanical and Control Engineering
Baicheng Normal University
Baicheng 137000, China

T. Zhou
Department of Civil
Environmental and Mining Engineering
The University of Western Australia
35 Stirling Highway, Crawley, WA 6009, Australia
E-mail: tongming.zhou@uwa.edu.au

The ORCID identification number(s) for the author(s) of this article can be found under https://doi.org/10.1002/smll.202511426

DOI: 10.1002/smll.202511426

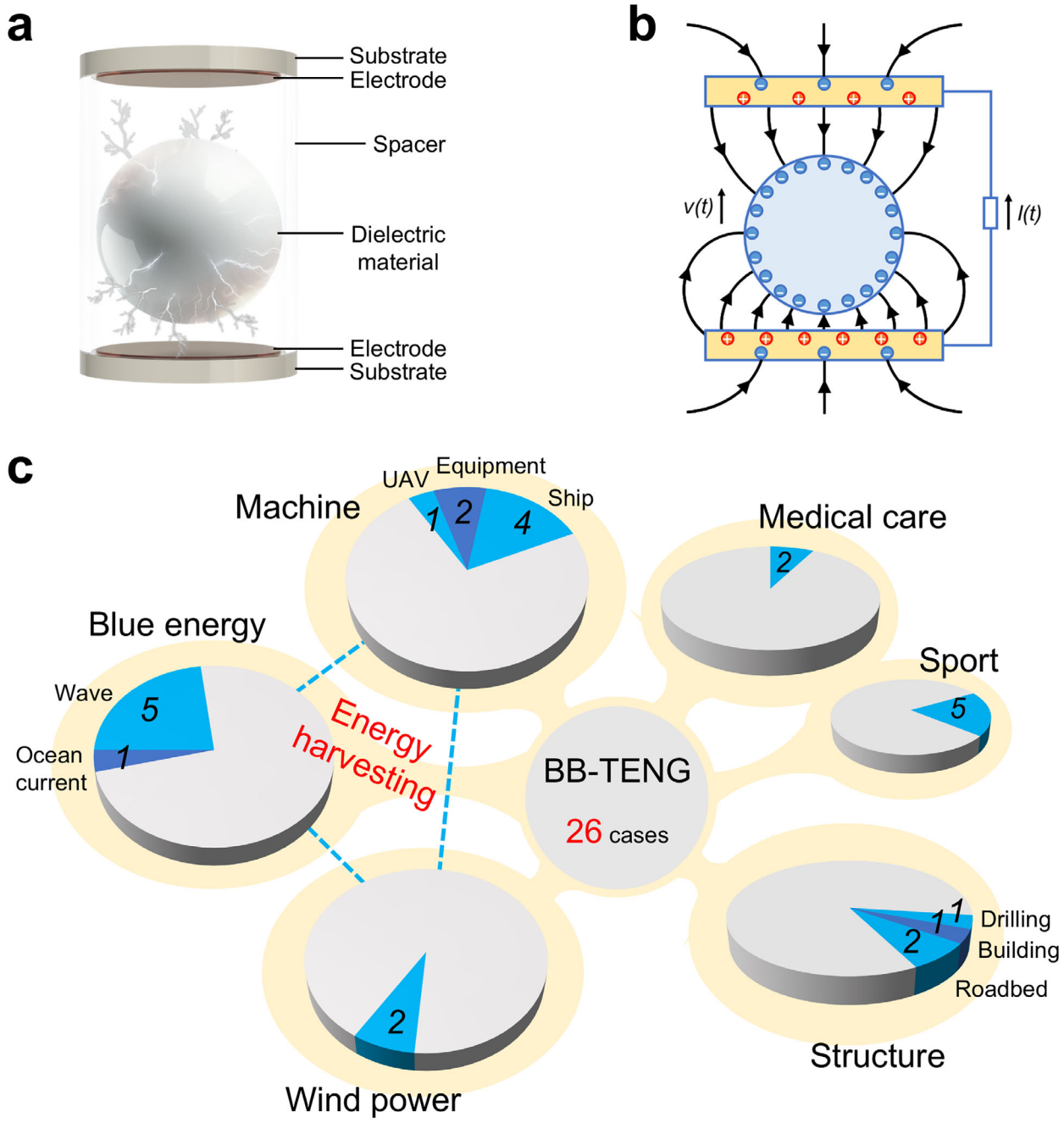

Figure 1. Schematic of the freestanding-layer-mode bouncing ball TENG. a) General structure. b) Charges distribution and electric field. c) Example applications of bouncing ball structured TENGs.

efficiently harvest mechanical energy across a broad range of vibration conditions. Consequently, BB-TENGs have been developed for extensive applications, including shipping,[12,13,21,22] unmanned aerial vehicle (UAV),[23] civil engineering,[15,16,24] wind power,[25,26] blue energy,[27–30] and medical care,[17,31] etc. Among the studies shown in Figure 1c, we were the first to design the classical sandwich structured BB-TENG (Figure 1a) and applied it to vibration energy harvesting and self-sensing of marine machinery.[12,21] The BB-TENG shows a high signal-to-noise ratio across most vibration ranges encountered in ship machinery.

Building on the above concept, Wang et al.[23] assembled three BB-TENG units into a triaxial vibration sensor for real-time monitoring of structural faults in UAVs. Cao et al.[25] and Wang et al.[26] developed fully packaged vortex-induced vibration TENGs, incorporating BB-TENGs as internal power generation units to scavenge wind energy from arbitrary directions. Wu et al.[32] and Zhu et al.[16] proposed spherical cavity structures with the ball arranged inside to absorb full-space vibration and shake from drilling and buildings for harvesting and monitoring. Zhu et al.[28] and Wang et al.[27] further adapted and stacked the

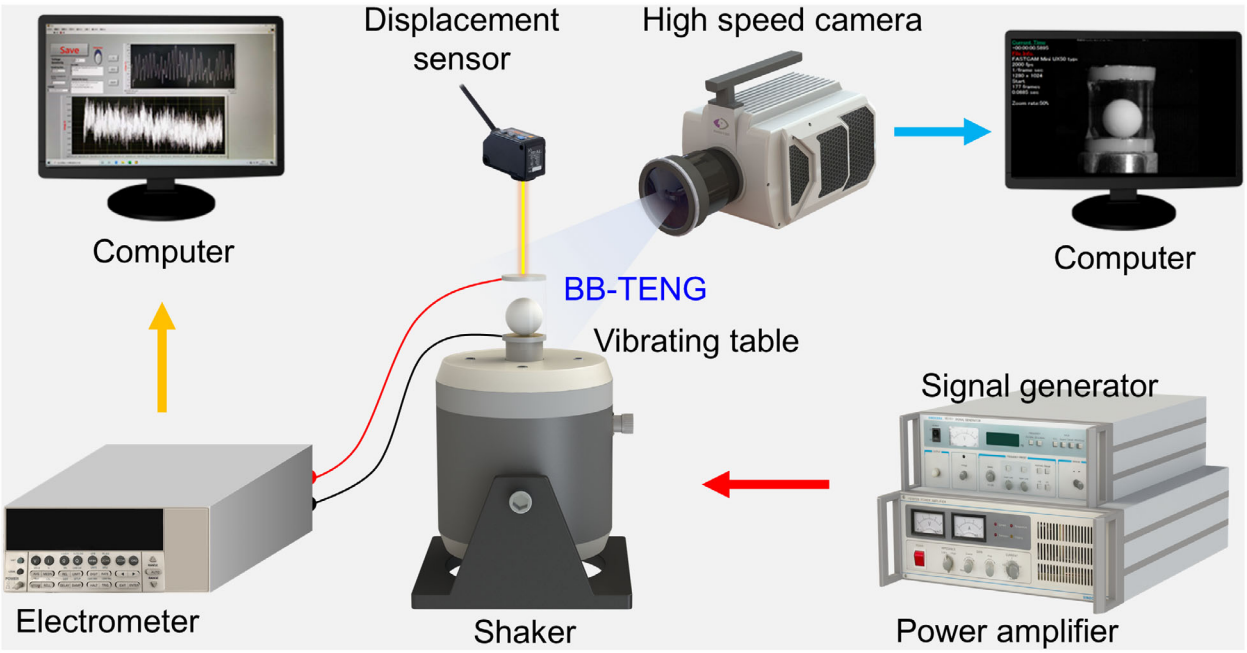

Figure 2. Experimental setup for simultaneous dynamic and electrical performance testing.

ball TENGs into ocean buoys to achieve extreme-low frequency wave energy collection and long-distance wireless communication in the real ocean environment. Furthermore, capsule-type BB-TENGs have been adopted in biomedical energy harvesting, for instance, Liu et al.[17] demonstrated a self-powered intracardiac pacemaker sustained by heartbeat-induced pellet motion.

Despite these advances in BB-TENG configurations and scenarios, the forced motion behaviors of the bouncing ball in the BB-TENGs have not been clearly elucidated. Most prior studies assume simple harmonic motion, which limits precise electromechanical coupling analysis, especially at the present stage, a decade after the triboelectric effect was first proposed.[33] The motion states (e.g., position, velocity, and acceleration) of the generator core (as the bouncing ball) are the prerequisites for accurately describing the electromechanical conversion in freestanding-layer mode TENG (such as the BB-TENG). Precise analysis, in turn, underpins for the effective TENG design and optimization.[34] As a result, a clearer motion process description and a proven electromechanical conversion mechanism will enable accurate predictions for TENG performances. However, both remain unresolved issues for the precise analysis of TENGs. In addition, experimental parametric studies often require numerous controlled-variable trials, which are costly and inefficient for design optimization.

In this study, a systematic analysis of the BB-TENG is presented, including the theoretical models, simulation methods, validation approach, and application analysis. The study further considers a bouncing ball moving between two electrode plates mounted on a vertically vibrating table, and derives the relationship between the dynamic responses of the ball and the key system parameters, including the vibration conditions, the restitution coefficient, the distance between two plates, and the diameter of the ball. Tracking by a high-speed camera, the dynamic behaviors of the bouncing ball are replicated in the Automatic Dynamic Analysis of Mechanical Systems (ADAMS) software. Four typical motion states associated with the BB-TENG electricity generation are confirmed after going through all the experiments. The measurements show that the electrical output of the BB-TENG coincides with the dynamic response of the bouncing ball system, providing validation for the superior linearity of the freestanding-layer mode. Building on this, and incorporating the electrostatic field calculation from the COMSOL Multiphysics software, a dual simulation coupling method is proposed, which is capable of accurately predicting TENG output. Finally, a recent application example using the proposed method is analyzed, providing a practical paradigm for the design and optimization of TENGs in real-world applications.

2. Dynamics of Bouncing Ball System

2.1. Experimental Setup

As illustrated in **Figure 2**, a dynamic and electrical characteristics test system is set up to evaluate the performance of the BB-TENG. An electromagnetic shaker (JZK-50) is driven by sine waves from a function generator (UTG2062B) and a power amplifier (YE5874A). The BB-TENG harvests energy from the vibrating of the shaker's table. A laser displacement sensor (HG-C1050) is suspended above the BB-TENG to measure the vibration amplitude. A high-speed camera (PHANTOM V2012) captures the motion state of the bouncing ball and streams real-time images to a computer. The electrical output from the BB-TENG is recorded to the computer using an electrometer (Keithley 6514).

The configuration of the tested BB-TENG, shown in **Figure 3a**, consists of a container and triboelectric layers. The container is formed by two parallel acrylic circular plates and a sandwiched

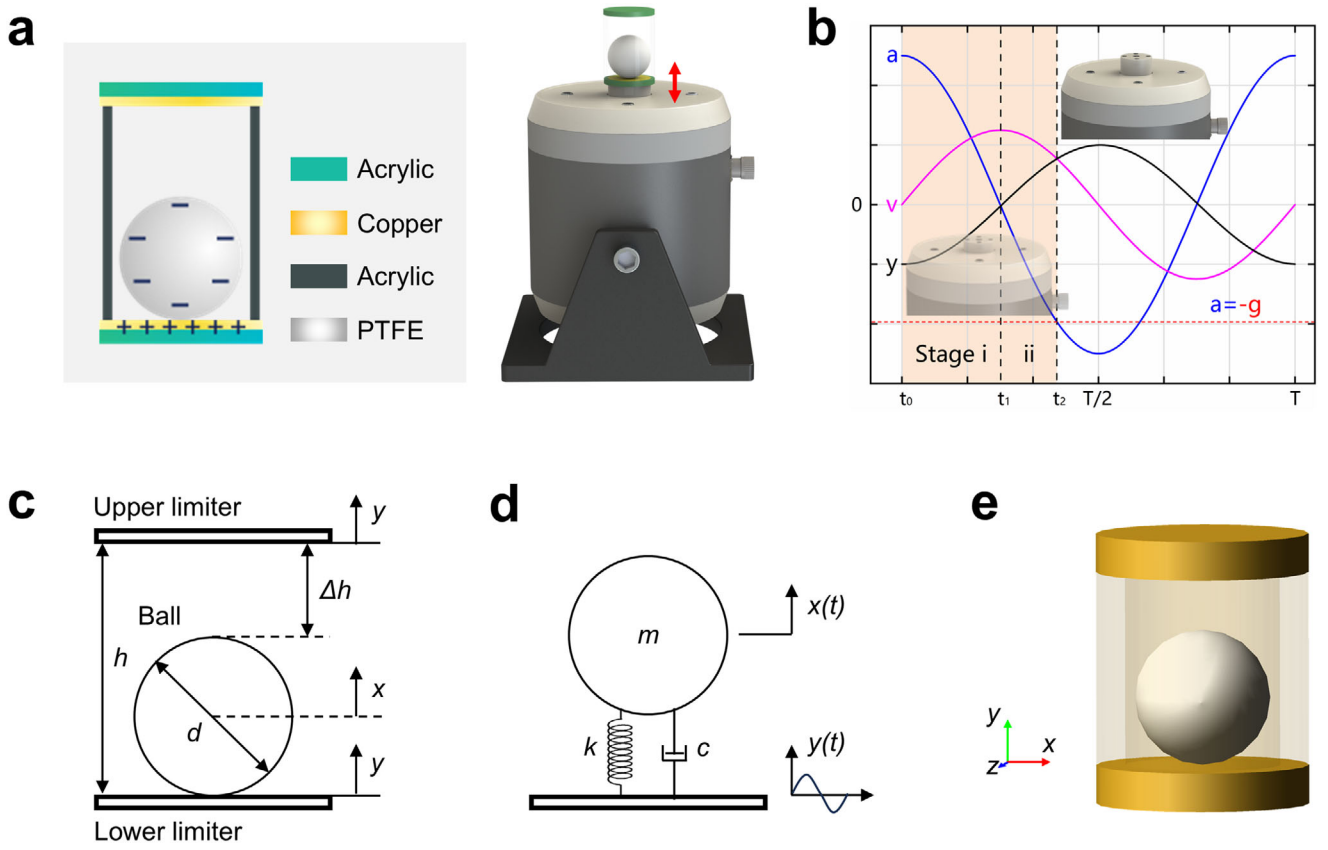

Figure 3. Bouncing ball system model under vertical vibration excitation. a) Configuration of the BB-TENG (Adapted with permission.[21] Copyright 2021, MDPI). b) Motion mode of the vibrating table. c) Bouncing ball system with two limiters. d) 1-DOF spring-mass-damper model. e) Multi-body dynamics simulation in ADAMS.

acrylic cylindrical tube, which together limit and guide the ball to move vertically. The polytetrafluoroethylene (PTFE) ball inside the container acts as the electronegative freestanding layer. The electropositive triboelectric layers consist of an upper copper electrode attached to the bottom of the acrylic plate and a lower copper fixed electrode bonded to another plate. The BB-TENG is glued to the shaker table via its container to maintain the consistency of their movement. The horizontal wandering of the ball is limited by the leveling of the vibrating table and by the concave surface colliding with the copper electrode. The geometric parameters of the BB-TENG can be found in **Table 1**.

When the BB-TENG is subjected to vertical vibration, the ball gains energy from the vibrating table and bounces accordingly. The vibrating table generates sinusoidal vibration with adjustable frequency and amplitude, as shown in Figure 3b. According to this simple harmonic motion, the vibration displacement y of the table can be expressed as $y = A\sin(\omega t + \varphi)$. Hereafter, A is the vibration amplitude, $\omega = 2\pi f$ is the angular frequency, f is the vibration frequency, t is the transient time, and φ is the initial phase angle. The vibration velocity v and acceleration a can then be denoted as $v = A\omega\cos(\omega t + \varphi)$ and $a = -A\omega^2\sin(\omega t + \varphi)$, respectively.

2.2. Theoretical Model

For simplicity, a one-degree of freedom (1-DOF) bouncing ball system with two rigidly connected limiters is used to characterize the dynamic behaviors of the BB-TENG on the vibrating table,

Table 1. System parameters of the BB-TENG model.

Component	Diameter × thickness × height [mm × mm × mm]	Material	Poisson's ratio	Young's modulus [N mm^{-2}]	Density [kg mm^{-3}]
Upper plate	*11 × 2*	PMMA	0.35	3200	1.19×10^{-6}
Lower plate	*11 × 2*	PMMA	0.35	3200	1.19×10^{-6}
Middle tube	*11 × 1.5 × 10*	PMMA	0.35	3200	1.19×10^{-6}
Ball	*7*	PTFE	0.4	400	2.2×10^{-6}

as shown in Figure 3c. Here, h denotes the distance between the two plates, d represents the diameter of the ball, and Δh is defined as the spacing between the ball and the upper plate at rest, which is generally expressed as $\Delta h = h - d$. Following common practice,[35] the mass of the vibrating table is assumed to be much larger than that of the bouncing ball, such that the table and the plates move independently of the ball's motion. The motion of the ball can be pre-analyzed using the motion curve in Figure 3b and physical experiences. In the first stage, the vibrating table begins to move upward from -A, with the ball resting on the lower plate and moving in sync with it. During this phase, the velocity v increases from 0, while the acceleration a is positive and decreases until the table reaches the zero-displacement position. In the second stage, the ball continues moving upward with the table from 0. Here, v decreases from the maximum value, and a increases in the downward direction from 0 until the ball's acceleration a_{ball} reaches the gravitational acceleration -g. However, the value of a_{ball} never exceeds the acceleration of the vibrating table. At this point, the ball leaves the lower plate and undergoes uniform deceleration under gravity -g until it collides with the upper plate. Under the given vibration excitation, the ball can collide with the upper and lower plates repeatedly.

The 1-DOF spring-mass-damper model is illustrated in Figure 3d. The displacements of the lower plate and the ball at time t are defined as $y(t)$ and $x(t)$, respectively, with $y(t) = A\sin\omega t$ for simplicity in the derivation. The relative displacement between the ball and the plate is defined as $z(t) = x(t) - y(t)$. The equation of motion of the bouncing ball with mass m is governed by $m\ddot{x} = -mg + \lambda(t)$,[35] where $\lambda(t)$ is the contact force between the ball and the plates. (1) When the ball stays on the lower plate and is forced to move, $z(t) = 0$, and $\lambda(t) = m\ddot{y} + mg$. (2) Once the ball leaves the plates ($0 < z(t) < h - d$), under the sole influence of gravity, $\lambda(t) = 0$ and the impulse-free dynamics is given by $m\ddot{x} = -mg$. (3) The impacts are modelled using the Hertz impact theory.[36] The impact dynamics can be derived directly to,

$$\lambda(t) = \begin{cases} -k(x - y - h + d) - c(\dot{x} - \dot{y}), \text{if } x > y + h - d \\ k(y - x) + c(\dot{y} - \dot{x}), \text{if } x \le y \end{cases} \tag{1}$$

where c and k are the damping coefficient and the contact stiffness, respectively. The bouncing ball system with limiters might exhibit more complex dynamic behaviors due to the non-autonomous nonlinearity introduced by the vibrating table.[35,37] In the present analysis, the ball interacting only with the movable lower plate is considered.

We assume that the time instant of the collision with the plate is t_n ($n \ge 1$), and the velocities of the ball before and after the collision are v_n^- and v_n^+, respectively. The condition for the subsequent collision is then given by:[37]

$$\begin{cases} v_n^+(t_{n+1} - t_n) - \frac{1}{2}g(t_{n+1} - t_n)^2 = A\sin(\omega t_{n+1}) - A\sin(\omega t_n) \\ v_{n+1}^- = v_n^+ - g(t_{n+1} + t_n) \end{cases} \tag{2}$$

And v_{n+1}^+ is further determined by the Newton-type of restitution law:[38]

$$\begin{cases} v_{n+1}^+ - \dot{x}(t_{n+1}) = -\varepsilon(v_{n+1}^- - \dot{x}(t_{n+1})) \\ \frac{c}{2\sqrt{mk}} = -\frac{\ln\varepsilon}{\sqrt{\ln^2\varepsilon + \pi^2}} \end{cases} \tag{3}$$

where ε is the restitution coefficient satisfying $0 \le \epsilon < 1$. After nondimensionalizing, Equations (2) and (3) can be expressed as:

$$\begin{cases} \Gamma\sin\left(\tau_n + \Delta\tau_{n+1}\right) - \Gamma\sin(\tau_n) = \chi_n^+\Delta\tau_{n+1} - \frac{1}{2}\Delta\tau_{n+1}^2 \\ \chi_{n+1}^+ = -\varepsilon\left(\chi_n^+ + \tau_n\right) + (1+\varepsilon)\Gamma\cos\left(\tau_n + \Delta\tau_{n+1}\right) \end{cases} \tag{4}$$

where τ_n and $\Delta\tau_{n+1}$ denote the nondimensionalized time and satisfy $\begin{cases} \tau_n = \omega t_n \\ \Delta\tau_{n+1} = \tau_{n+1} - \tau_n \end{cases}$, and $\chi_n^+ = v_n^+\omega/g$ is the nondimensionalized velocity. The parameter Γ is related to the amplitude and frequency of the vibration excitation by $\Gamma = A\omega^2/g$.

If the ball and the lower plate are to be continuously contacted and separated, the Lyapunov stability of the system must first be broken.[39] The Lyapunov stability interval trapping this system holds that,

$$0 < \gamma = \frac{g + A\omega^2}{g - A\omega^2}\varepsilon^2 < 1 \tag{5}$$

within which the ball cannot be separated from the lower plate under the external vibration, or will stay again on the lower plate after a finite number of collisions.[40]

According to Equations (1–5), the dynamic behaviors of the bouncing ball system with limiters are affected by the vibration intensity Γ, the restitution coefficient ε, the distance between the two limiters h and the diameter of the ball d. It is generally recognized that ε depends on the mechanical properties of the material itself,[41] such as the Poisson's ratio and Young's modulus. It is noted that the balls and the plates employed in this study are the same batch of products from the same manufacturers, ensuring material consistency. This study examines how the vibration conditions (including f, A and a) and the structural parameters (including h and d) affect the motion modes of the BB-TENG. More detailed dynamical models for a ball bouncing between two limiters, exhibiting a variety of complex and interesting behaviors, have been reported by Lampart et al.[36] and Li et al.[35,39]

Accurate solving the impulsive dynamics of non-smooth mechanical systems remains a challenge.[36] Observing the motion of an internal bouncing ball within a closed device undergoing high-speed vibrations is equally difficult, and direct measurement is even more challenging. In this study, the commercial software ADAMS is employed to simulate the BB-TENG and replicate the behaviors of the bouncing ball. As shown in Figure 3e, the multi-body dynamics model adopts the typical sandwich structure for the BB-TENG. The upper and lower plates and the middle tube made of the polymethyl methacrylate (PMMA) material are fixed together using Boolean operations. The bouncing ball with a smaller diameter is modeled as a rigid body made of PTFE. The thickness of the copper electrodes after repeated impact in this studied system is considered to be negligible relative to that of the plates. Nevertheless, Coulomb friction corresponding to copper-PTFE contact is applied when the ball is in contact with the plates. The geometric parameters and material properties are listed in Table 1.

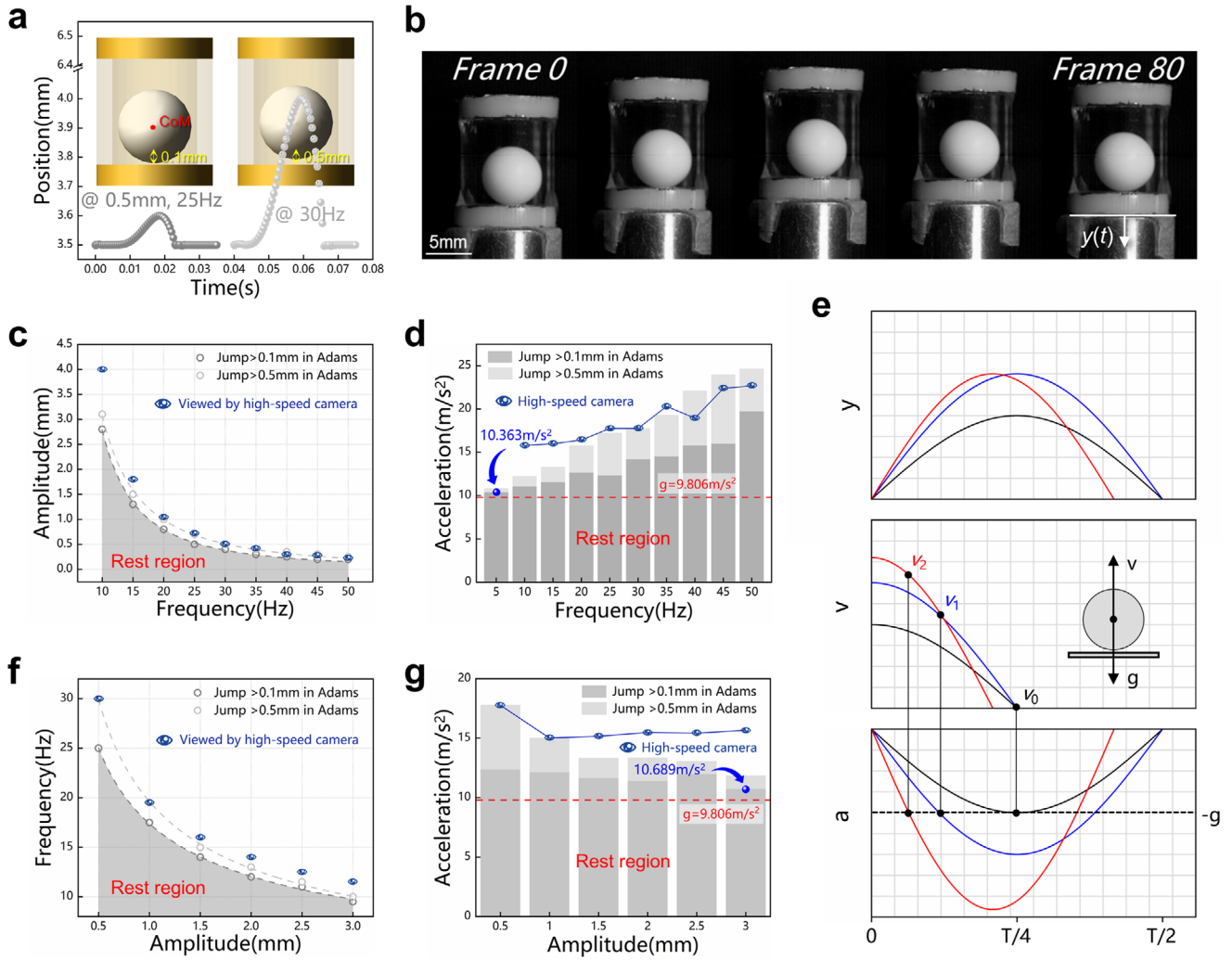

Figure 4. Bounce of the bouncing ball. a) Time series of the bounce using simulation. b) Continuous images of the bounce process obtained using camera. c) and d) Onset of the bounce from simulation and experiment at various frequencies. e) The *y*-*v*-*a* curves in the sinusoidal motion of the vibrating table. f) and g) Onset of the bounce from simulation and experiment at various amplitudes.

2.3. Dynamic Behaviors of Bouncing Ball under Vibration Excitation

The simulation results under different vibration excitations reveal periodic, quasi-periodic, and chaotic patterns, consistent with the oscillatory behaviors described in ref. [36] In this study, the primary dynamic behaviors of the PTFE ball as the freestanding layer in the BB-TENG are focused on its bounce, chaos, critical contact, and regular contact. According to the basic working principle of TENGs, the displacement current is generated when the dielectric layer and the electrode undergo contact and separation.[42] In this contact-mode,[43] full contact between the freestanding layer and both electrodes ensures complete short-circuit charge transfer. Therefore, whether the ball bounces only on the lower plate or also contacts the upper plate determines the lower or upper bound of energy harvesting. Regular contact with the upper plate yields the maximum stable output, whereas chaotic motion leads to a fluctuating electricity generation.

2.3.1. Bounce Dynamics

In the freestanding layer mode, the electricity conversion of the BB-TENG relies on the ball bouncing off the lower plate.[12] The bounce condition is first examined using ADAMS software. **Figure 4a** shows the positions of the ball's center of mass (CoM) relative to the center of the lower plate. For example, if the position of CoM is shifted from 3.5 to 3.6 mm, its displacement is recorded as 0.1 mm, indicating that the ball has left the lower plate and begun bouncing. In this case, the frequency *f* of the vibrating table is set to 25 Hz and the amplitude *A* is 0.5 mm. To validate the simulation, a high-speed camera is used to capture the real-time motion of the ball. A series of continuous images showing the bounce process is shown in Figure 4b and Video S1, Supporting Information, with frames sampled every 20 frames at a rate of 2000 fps. It can be observed that the ball exhibits an obvious relative displacement from the lower plate in the 80th frame after the vibrating table moved up. For easier visual identification in the camera images, a larger displacement of 0.5 mm

is also adopted as the jumping point in the simulated case with $f = 30$ Hz and $A = 0.5$ mm, as shown in Figure 4a.

The influence of vibration frequency and amplitude on achieving ball bouncing is further investigated using the proposed simulation model. Since most machinery operates at low rated frequencies,[7] the shaker frequency range in this study is set to ≈0–50 Hz, considering the operational limit of the shaker. Figure 4c shows the minimum amplitude required for ball to jump at different vibration frequencies. The shaded area below the curve of 0.1 mm represents the rest region where the ball cannot lift off and no electricity output is generated. In contrast, the blank area above the 0.5 mm curve indicates that the ball starts to jump. For instance, at 5 Hz, the required amplitudes are 10.5 and 11 mm respectively, which greatly exceeds the maximum limit of the shaker, being hidden in Figure 4c but can be found in Table S1, Supporting Information. Then, each simulated jump point is taken as the initial input of the shaker. The behaviors of the bouncing ball in a transparent tube are recorded using high-speed camera to identify the actual jump points in surrounding areas. The camera-verified points are distributed close to the two simulated curves ranging from 10 Hz to 50 Hz in 5 Hz increments, with a bias toward the one of 0.5 mm, as the larger displacement is easier to observe. Photographs of the justified jump moments are provided in Figure S1, Supporting Information, which partially verifies the proposed simulation model.

For the bounce condition, previous research[40] and our analysis indicate the followings: when the bouncing ball stays on the lower plate moving along, it will only leave the plate and move upward when the vertical acceleration of the vibrating table acting on the ball is equal to the gravitational acceleration g. Later, the acceleration of the vibrating table continues to increase and exceeds the gravitational acceleration, the ball begins its free-flight motion. As $a = -A\omega^2 \sin(\omega t + \varphi)$, the maximum acceleration that the vibrating table can achieve is.

$$|a_{max}| = A\omega^2 = A(2\pi f)^2 \tag{6}$$

The coordinate (f, A) of the jump point is the excitation condition for the vibrating table. All points from simulation and verification are substituted into Equation (6), and the results are plotted in Figure 4d. The minimum calculated acceleration is 10.363 m s^{-2}, occurring at 5 Hz and 10.5 mm, which is also slightly greater than $g = 9.806$ m s^{-2}, verifying the proposed bounce condition. The reason why all the acceleration eventually exceeds g can be revealed by the sinusoidal motion curves in Figure 4e. Before T/4, The bouncing ball moves upward with the vibrating table in a deceleration motion but with increasing acceleration, as displayed in the black curves. If the maximum acceleration of the table in one cycle only reaches -g and the corresponding velocity is reduced to 0, it will not be able to provide the initial velocity v_0 for the bouncing ball with the same -g to separate from the lower plate. Therefore, it is necessary to ensure that the vibration table still retains a certain velocity when its acceleration is -g, as shown in the blue lines and the schematic in Figure 4e. Under this condition, the ball can successfully escape from the plate. And then, the maximum acceleration will be obtained when the table also decelerates to 0 and satisfies $|a_{max}| > g$.

Correspondingly, both simulations and experiments are conducted to determine the ball's jumping frequencies at fixed vibration amplitudes. Figure 4f,g shows the excitation frequency and vibration intensity required for the ball to jump for the amplitude ranging from 0.5 to 3 mm. The verified points are also close to the fitted curve of 0.5 mm, in which the coordinates of (0.5 mm, 30 Hz), (1 mm, 19.5 Hz) and (1.5 mm, 16 Hz) are cross-checked with Figure 4c to avoid contingency. In Figure 4g, the weakest vibration intensity represented by $|a_{max}|$ is calculated to be 10.689 m s^{-2}, which also exceeds g. Table S2 and Figure S2, Supporting Information present a quantitative and visual summary of all the coordinates, showing that the simulated results are in good agreement with the experiment data.

After jumping (i.e., $0 < z(t) < h - d$), the ball undergoes vertical projectile motion, described by the displacement formula:

$$x(t) = v_0 t - \frac{1}{2} g t^2 \tag{7}$$

where the displacement $x(t)$ is proportional to v_0. As shown by the blue or red curves in Figure 4e, during the rising and decelerating stage, the earlier the vibrating table reaches a = -g, the higher the remaining v_0 of the ball. To achieve this, the amplitude or frequency input of the vibrating table need to be increased. In this case, as indicated by Equation (6) and Figure 4e, the maximum acceleration of the table increases accordingly. This can explain why at high frequencies, the vibration intensity of the table can far exceed g, reaching up to 24.674 m s^{-2}. In Equation (6), when the bounce condition $|a_{max}| \approx g$ is fixed, the amplitude of the table decreases with the inverse square of its frequency as the frequency gradually increases. According to Equation (8),

$$|v_{max}| = 2\pi A f \tag{8}$$

the velocity of the vibrating table is smaller at higher frequencies. As analyzed above, the vibration intensity must be further increased to make the ball jump as early as possible and to maximize its initial velocity. As shown in Figure 4d,g, the required acceleration increases as the table's velocity decreases.

Besides, it can be observed that the visual values at 10 Hz in Figure 4c and 3 mm in Figure 4f differ significantly from the simulation results. This discrepancy may be attributed to the visual error. With an acceleration is approximately g, the velocity of the vibrating table during jump is similar to that of the ball, making their relative displacement difficult to detect. An important corroboration is that almost all the jumping displacements are captured by the high-speed camera when the vibrating table is descending, rather than the rising stage, as seen in Frame 80 of Figure 4b. An important finding of Yu[44] may reply to our concerns, in that the restitution coefficient ε after a collision is not a material constant but is closely dependent on the impact velocity. When an elastoplastic structure (such as the real PTFE ball in this study) impacts a solid wall, its plastic deformation dissipates the total kinetic energy of the system. The offset points mentioned here correspond to large velocities according to Equation (8) and satisfy $\epsilon < 1$ in this bouncing ball system. Meanwhile, Yu noted that oblique collisions with friction present a more complex mechanical problem whose mechanisms are not yet fully understood. In a real experimental system, the ball cannot bounce vertically in a fixed place because of the imbalance of the table and the imperfection in the ball. Lateral shift is inevitable,

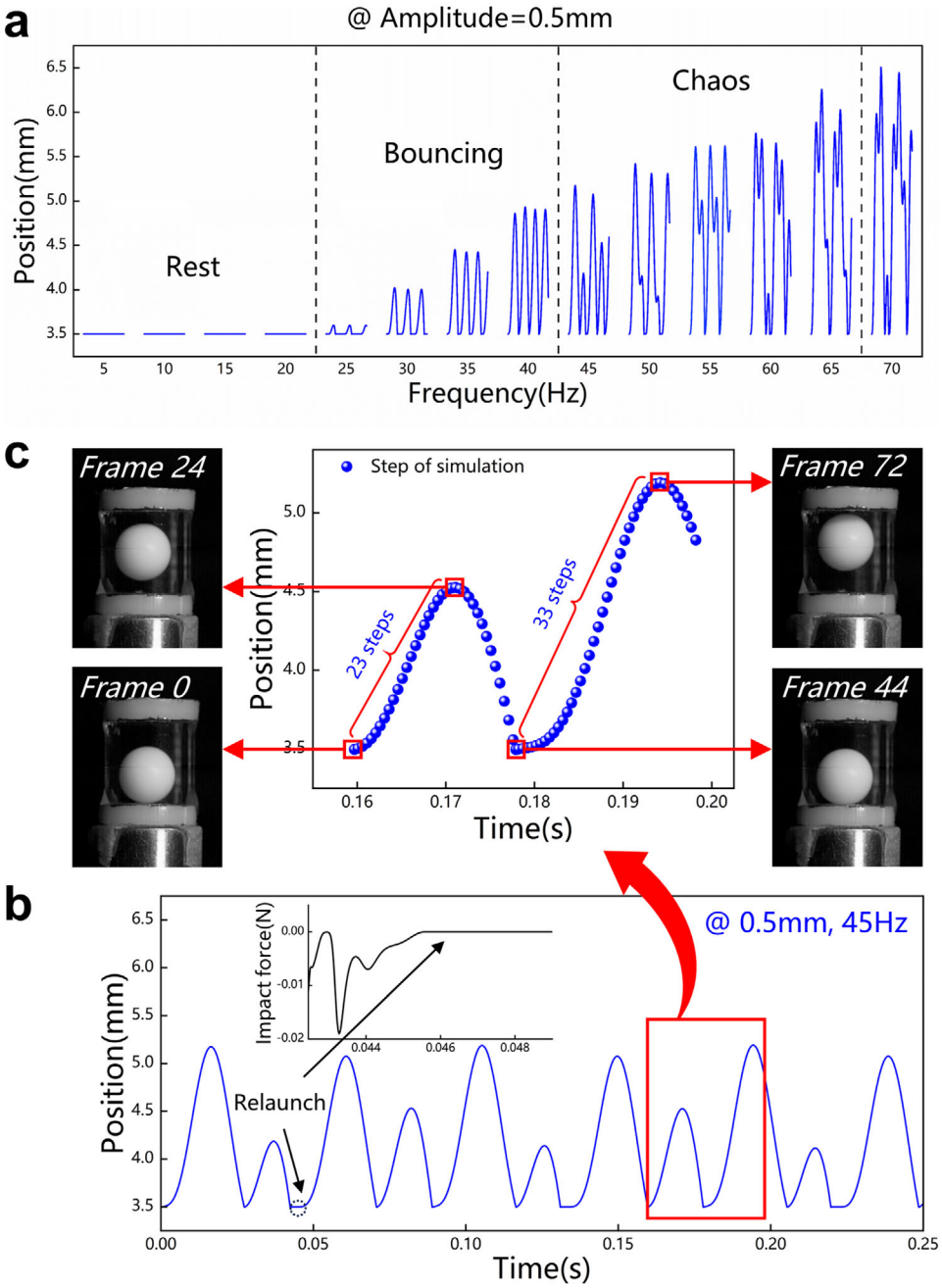

Figure 5. Chaos of the bouncing ball. a) Simulation results at various frequencies with a fixed amplitude of 0.5 mm. b) Motion details in the simulation at 45 Hz. c) Photographs of the chaotic behavior.

especially at low frequencies and large amplitudes, where the ball may roll around or even lean against the tube. This issue has also been noted in ref. [40]. The presence of air inside the cell imposes an additional damping effect on the ball's motion due to air resistance, which further reduces the restitution coefficient and the maximum jumping height. Due to the scope and focus of the present study, these considerations are not explored here, but they remain worthy of future investigation.

2.3.2. Chaos Dynamics

As the added amplitude or frequency of the vibrating table increases, the jumping height of the bouncing ball gradually increases until it touches the upper plate. **Figure** 5a shows the simulated trajectories for driving frequencies from 5 to 70 Hz at a fixed amplitude of 0.5 mm. In the range of ≈25–70 Hz, the maximum displacement increases almost linearly from 0.09 to 3 mm, with a fitted curve yielding an R^2 value of 0.98, as quantized in

Figure S3, Supporting Information. The condition for the ball to leave the lower plate can be expressed as:

$$\begin{cases} a_0 = -A\omega^2 \sin(\omega t_0 + \varphi) \\ v_0 = A\omega \sin(\omega t_0 + \varphi) \end{cases} \quad (9)$$

where $a_0 = -g$ is the theoretical table acceleration at which the ball can be flung off. At this point, the initial velocity of the ball, or the remaining velocity of the table, can be calculated as:

$$v_0 = \frac{\sqrt{A^2\omega^4 - g^2}}{\omega} \quad (10)$$

Combined with Equation (7), the jumping height $x(t)$ of the bouncing ball is proportional to ω, which explains the linearly increasing trend observed in Figure 5a.

After bouncing, the chaotic behaviors of the bouncing ball are often observed,[40,45,46] as shown in Figure 5a. The mechanisms responsible for the chaos are still in dispute. In a simple case, a ball dropped onto a table will bounce repeatedly with the bouncing height being smaller and smaller until it comes to rest. As the collisions between them are inelastic, the ball loses a fraction of energy in each collision. When the table is vibrated vertically, as in this study, the ball can bounce indefinitely by gaining energy from the vibrating table. However, if the excitation is insufficient, such as when the ball enters into the vibration phase with a relatively small velocity, it may become locked onto the table through an infinite sequence of smaller and smaller bounces in a finite time, and then be relaunched from the vibrating table at an appropriate time.[46] In addition to the external perturbation, such as the imperfections from itself and the table, and the sliding friction from the tube, etc., which can themselves cause the chaotic behavior of the ball, Jiang et al.[40] have also reported the velocity-dependent collision duration can disrupt the sequence of diminishing bounces to induce the chaos. In their results, the collision duration increases with the decreasing collision velocity v_n^-, thereby destroying the sticking solutions. In Figure 5a of this study, the calculated velocity from Equation (8) below 0.22 m s^{-1}, which falls within their measurement range. At 45 Hz, the collision duration is longer according to ref. [40]. As shown in Figure 5b, after performing the first two bounces, the bouncing ball loses most of its kinetic energy, causing it not to jump immediately but to stay on the plate waiting for the next relaunch. The relaunching mechanism makes the ball's simulated trajectories appear periodic.[45,46] The inset of Figure 5b indicates that, after the second small bounce, the impact force varies in a damped oscillatory and the remaining energy is dissipated. In this case, the subsequent chaotic behavior of the bouncing ball is captured by the high-speed camera (see Video S2, Supporting Information), with some typical positions displayed in Figure 5c. Four photographs capture the ball performing two chaotic bounces. Corresponding to the sampling rate of 2000 fps, the step size of the simulation is set to 1/2000 = 0.0005 s. In the simulation result, the bouncing ball reaches the first peak from the initial position after 23 steps, and 33 steps elapse from the second contact with the lower plate to the second peak. The 70-step process is validated by two distinct motion changes observed in Frames ≈0–24 and Frames ≈44–72. A notable deviation occurs only in determining the simulation step for Frame 44, which corresponds to the jumping, likely due to a visual error similar to that noted earlier. Overall, the simulation closely reproduces the trajectory of the actual motion.

In all the visual experiments, chaos caused by external disturbances is common but does not obscure the major motion. Chaos induced by interruption of stiction tends to occur in the vibration conditions with small amplitudes but higher frequencies, such as in Figure 5a where the input frequency ranges from 45 Hz to 70 Hz at the amplitude of 0.5 mm. In this condition, low velocities are caused by small amplitudes, but from Equation (6), the higher frequencies also result in large accelerations. The rapid alternation in both magnitude and direction of the oscillatory acceleration prevents the relaunching phase from remaining fixed.[40] Arguing here that it is this fluctuation that induces the chaos of the bouncing ball. In the chaos, the electrical output of the BB-TENG becomes unstable due to the irregular contacts and separations between the bouncing ball and the electrodes on the plates.

2.3.3. Critical Contact Dynamics

Only when the bouncing ball leaves the lower plate and arrives at the upper plate can the total short-circuit transferred charge amount in the BB-TENG be fully reached.[43] Ensuring the free-standing layer fully contacts the two electrodes is highly beneficial for harvesting the mechanical energy with maximum conversion efficiency. In this study, the contact conditions are simulated and verified using ADAMS software and high-speed camera. **Figure 6a** depicts the contact in the simulation, showing the ball strikes the upper plate under an appropriate vibration (10 Hz, 4.1 mm), with a CoM displacement of 3 mm. This minimal but complete contact with the upper plate is referred to as critical contact in this study, which is more vividly reflected by the trajectory at 70 Hz shown in Figure 5a. Critical contact forms the basis of generating maximum output for the BB-TENG. Corresponding to Figure 6a, the actual images of the critical contact behavior at 10 Hz and 4.4 mm are captured in Video S3, Supporting Information. Every 18 frames are recorded in Figure 6b. Following the bouncing ball observed to jump, its contact with the upper plate occurs in Frame 72. The detailed simulation results of this process are sampled in Figure 6c. As described earlier, after gaining velocity (pink line) from the lower plate, in the second stage of waiting for launch, the ball is thrown when the acceleration of the plate reaches $a = -g$. The launching velocity of 0.2 m $^{-1}$s in the simulation agrees well with the numerical solution of v_0 = 0.205 m $^{-1}$s from Equation (10). Entering the third stage corresponding to Figure 6b, the simulated ball takes 0.037 s to travel from the lower plate to the upper (black line), with a uniform deceleration motion due to gravity (pink and blue lines). The contact time, recorded as 72 frames in the high-speed camera, corresponds to 72 × 1/2000 = 0.036 s, validating the ADAMS simulation. The result in Figure 6c is consistent with the preliminary analysis in Section 2.2 of the ball's behavior.

The critical contact points at other fixed frequencies and amplitudes are displayed in Figure 6d and Figure S4, Supporting Information, respectively. When the ball exhibits a larger displacement, contact with the upper plate is easier to detect in time compared with jumping. It can be found that the

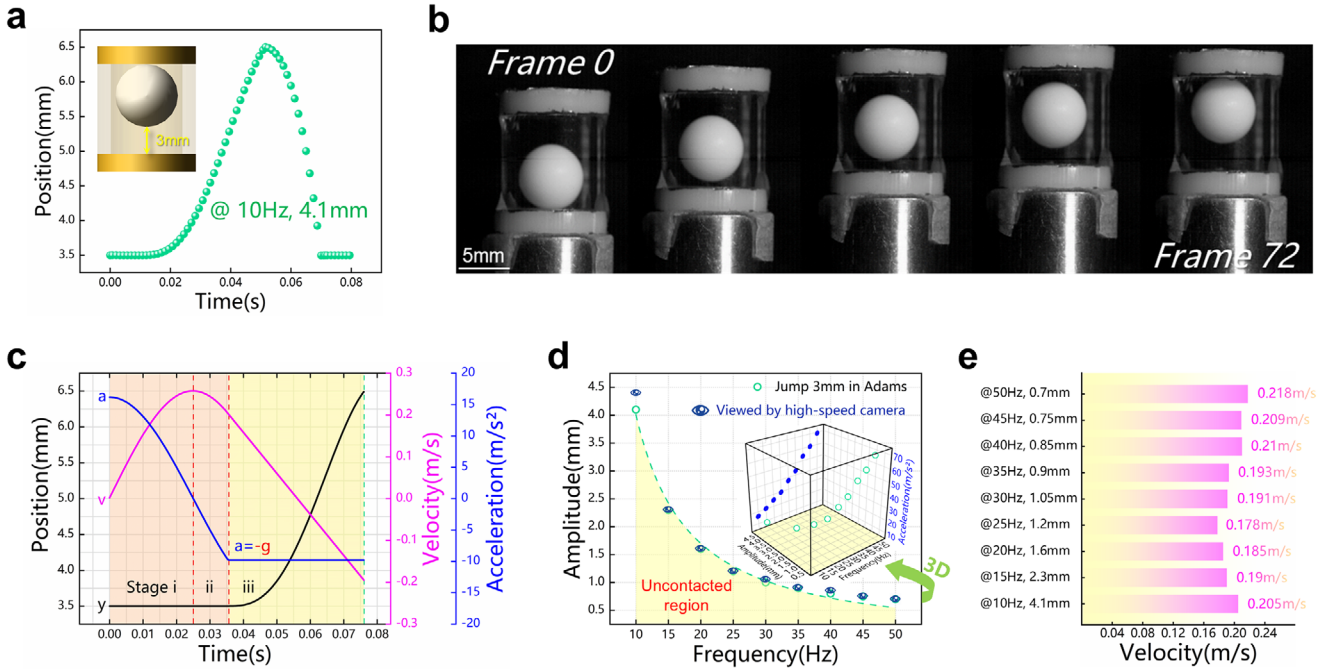

Figure 6. Critical contact of the bouncing ball. a) Time series of the critical contact using simulation. b) Continuous images and (c) simulation results of the critical contact behavior. d) Onset of the critical contact from simulation and experiment at various frequencies. e) Initial velocities of the bouncing ball leaving the lower plate under these conditions.

simulation results agree well with the experimental observations, with each validated key frame provided in Figure S5, Supporting Information. The colored area designates an uncontacted region encompassing rest, bouncing, and partial chaos regions that do not generate desirable outputs. Prior to any collision with the upper plate, the impulse-free dynamics of the bouncing ball is governed by Equation (10). Based on this relation, the calculated initial velocities v_0 tend to be consistent, as shown in Figure 6e, due to the same spacings Δh of 3 mm between the ball and the upper plate. Their difference comes from the movements of the upper plate which actively contacts the bouncing ball under different vibration conditions. In this case, according to $\begin{cases} v_0 \approx A\omega, \text{if } A^2\omega^4 \gg g^2 \\ |a_{\max}| = A\omega^2 \end{cases}$, the maximum acceleration of the vibrating table increases almost linearly with the frequencies ranging from 10 Hz to 50 Hz, as reflected in the 3D inset of Figure 6d.

We further investigate the effect of the spacing Δh and the diameter of the bouncing ball d on the critical contact with the upper plate using the proposed simulation and the visual experiment. The middle tubes with heights of 8, 9, 10, 11, and 12 mm are used to create various spacings while other structures remain uncharged. Figure S6, Supporting Information displays the simulation and experiment results for Δh = 1, 2, 3, 4, and 5 mm. It is noted that the required vibration intensity to achieve contact increases progressively with Δh, leading to a corresponding enlargement of the uncontacted region. For the diameter d, five common balls with diameters of 5, 6.35, 7, 8, and 10 mm are selected and analyzed at a fixed 3 mm spacing for bouncing. Accordingly, the diameters of the tubes and plates are also increased. As shown in Figure S7 (Supporting Information), both simulation and experiment results reveal that the critical contact conditions for different ball diameters d are essentially the same. This is because, compared with the lightweight BB-TENG, the excitation in both software or actual scene can be regarded as an infinite energy source, making the impact of the BB-TENG's mass on the vibration intensity is negligible. Therefore, the spacing Δh between the bouncing ball and the upper plate becomes a key parameter for the BB-TENG design.

2.3.4. Regular Contact Dynamics

By further increasing the frequency or amplitude for the vibrating table while the system is in critical contact, the bouncing ball transitions into regular contact with the two plates. In this well-contact condition, the BB-TENG achieves its maximum stable output due to full and consecutive separation of the short-circuit transferred charge amount. **Figure** 7a,b shows a regular-contact state of the bouncing ball at an amplitude of 3 mm and frequency of 30 Hz in the simulation result with photographs. In the representative process shown in Figure 7b, the bouncing ball departs from the lower plate after 21 simulation steps of contact, and then begins to fall through 20 steps in contact with the upper plate, which are consistent with the validation images of Frames ≈0–21 and Frames ≈37–57. This typical process consists of, twice contact and separations between the ball and two plates, four states shown in the selected photos, being easily distinguishable. And the total frames also correspond to the simulation steps of 59. As confirmed in Video S4, Supporting Information or in Frame 37 to Frame 57, $\gamma_2 < \gamma_1$, indicates that after contacting the upper plate, the BB-TENG moves downward, forcing the ball to move with the

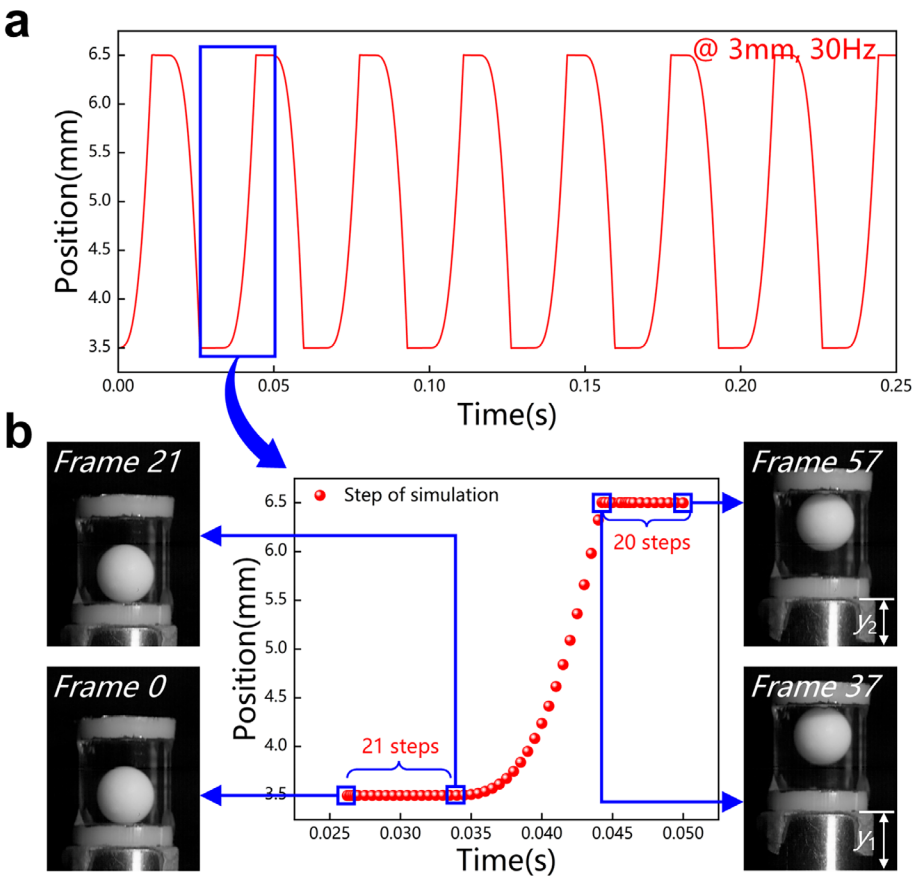

Figure 7. Regular contact of the bouncing ball. a) Simulated motion trajectory at 3 mm and 30 Hz. b) Motion details and its validation photographs.

plate and maintain continuous contact. Contact with the lower plate follows a similar but reversed process. Two plates alternate in this regular dynamic behavior, illustrated in Figure 7a. This sticking contact promotes sufficient friction between the bouncing ball and the electrodes on the two plates, ensuring effective charge transfer, and thus improving the output performance of the BB-TENG.

3. Electrification of BB-TENG

3.1. Working Principle

As shown in **Figure 8a**, a PTFE ball as the dielectric layer and two copper electrodes as the metal layers are stacked face to face, forming two triboelectric pairs. When the PTFE ball is forced to contact with the copper electrodes, the surface of the dielectric ball will have negative charges due to contact electrification [47] and triboelectric series.[48] As dimensioned in Figure 3c, the BB-TENG in this study can be represented by a classic capacitance series model,[43] from which the short-circuit transferred charges (Q_{SC}) and the open-circuit voltage (V_{OC}) between the upper and lower electrodes can be calculated as follows:

$$Q_{SC} = \frac{2\sigma S x}{d_0 + h - d} \tag{11}$$

$$V_{OC} = \frac{Q_{SC}}{C} = \frac{2\sigma x}{\varepsilon_0} \tag{12}$$

where σ, S, x, h, d, C, and ε_0 denote the initial charge density on the dielectric material, the contact area between the dielectric ball and the electrode, the separation distance, the total air gap thickness between two electrodes, the diameter of the dielectric ball, the total equivalent capacitance and the vacuum permittivity, respectively. The effective dielectric thickness d_0 is defined as $d_0 = d/\epsilon_r$ and ϵ_r is relative dielectric constant. From Equation (11) and (12), it is noted that both Q_{SC} and V_{OC}, the electrical output characteristics for the BB-TENG, have a linear relationship with the ball's vertical displacement $x(t)$. This linear dependence on $x(t)$ makes the BB-TENG an ideal transducer for converting mechanical energy into electricity, with potential applications in energy harvesting and self-driven sensing.[7]

The working principle of the BB-TENG over a complete cycle is illustrated in Figure 8a,b, based on the charge distribution models proposed by Zhao et al.[34] and Guo et al.[49] In Figure 8a(i), the contact between the negatively charged PTFE ball and the lower copper electrode attracts positive charges to the lower electrode. When vibration excitation lifts the ball away from the lower plate, an unbalanced potential difference is induced between the upper and lower electrodes. This drives charge transfer from the lower to the upper electrode, forming an upward electric current, as shown in Figure 8a(ii). If the vibration

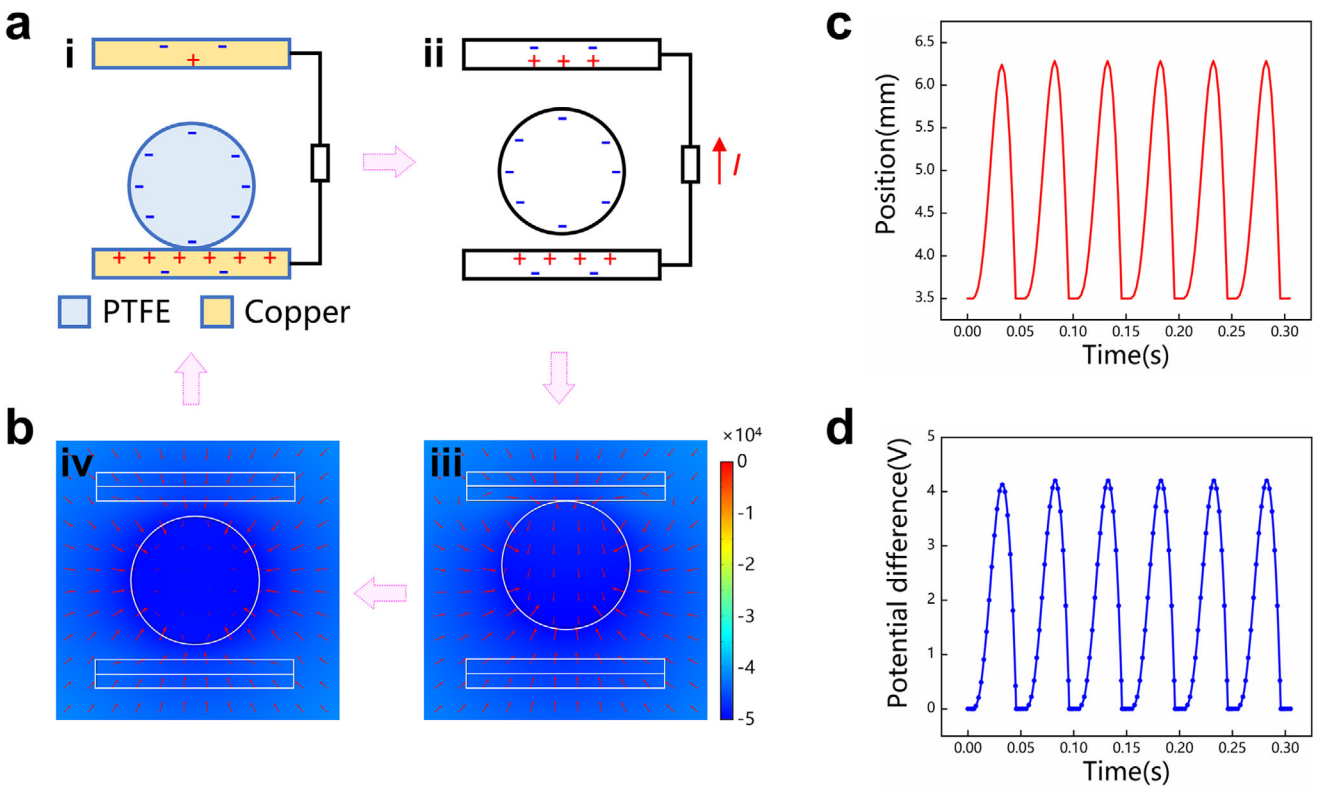

Figure 8. Working principle and simulation analysis of the BB-TENG. a) Schematic diagram of the triboelectric layers. b) Finite element simulation of the electric field distribution within the BB-TENG. c) Simulated motion trajectory of the bouncing ball using ADAMS software. d) Potential difference between the upper and lower electrodes, calculated in COMSOL software based on the data in (c).

is sufficient for the charged PTFE ball to contact with the upper electrode (Figure 8b(iii)), the total short-circuit transferred charges is reached, restoring the electrostatic equilibrium. A new potential imbalance occurs when the ball falls back under its gravity and the reactive force from the upper plate, as shown in Figure 8b(iv). Charges then flow back to the lower electrode, generating a reverse current until the PTFE ball contacts the lower electrode again (Figure 8a(i)). Through this process, the forced motion of the PTFE ball induces the alternating charge flow between the electrodes, resulting in an AC output as:

$$I_{SC}(t) = \frac{dQ_{SC}}{dt} = \frac{dQ_{SC}}{dx}v = \frac{2\sigma S v}{d_0 + h - d} \tag{13}$$

From Equation (13), the short-circuit current I_{SC} depends on the magnitude and direction of the ball's velocity v. This theoretical conclusion can also be verified by the experimental results in the following section.

Reasonable values of the charge density on the dielectric ball and the motion states are used for finite element simulations. Detailed settings can be found in **Experimental Section**. As shown in Figure 8b(iii),(iv), COMSOL simulations for two representative positions confirm the corresponding electric field distribution. Since the electrode distance is comparable to the BB-TENG size, the finite plate model proposed by Zhao[34] is also incorporated in the simulation. The resulting electric field inside the TENG (red arrows) demonstrates non-uniformity in both magnitude and direction. In addition, COMSOL was used to calculate the potentials on the independent electrodes induced by the charged ball. Figure 8c shows the displacement $x(t)$ of the bouncing ball over 5 cycles obtained from ADAMS simulations. For the case of $A = 1.5$ mm and $f = 20$ Hz, the ball almost touches the upper plate. These discrete positions are provided as the input to the theoretical model shown in Figure 8b, and the corresponding results are shown in Figure 8d. Under the open-circuit condition, the potential difference between the two electrodes is defined as V_{OC} of the TENG.[50] Here, its variation matches the motion curve in Figure 8c. This agreement verifies both the proposed charge transfer mechanism and the theoretical prediction in Equation (12). From the above discussion, it is clear that the motion of the freestanding layer directly governs the electricity generation in this TENG mode. This finding further demonstrates the value of analyzing the dynamic behaviors of the bouncing ball for optimizing the performance of ball-based nanogenerators.

Moreover, the introduction of dynamic simulation in this study provides more accurate feature inputs for predicting the BB-TENG performance, as its consistency with the actual motion has been verified in the previous section. Although the theoretical model and solution for the TENG have been rigorously derived, achieving accurate results ultimately depends on precise knowledge of the TENG's material charge distributions, internal distances, and actual motions.[34] As mentioned above, Zhao and Shao[34,49] determined the distribution of initial charges on

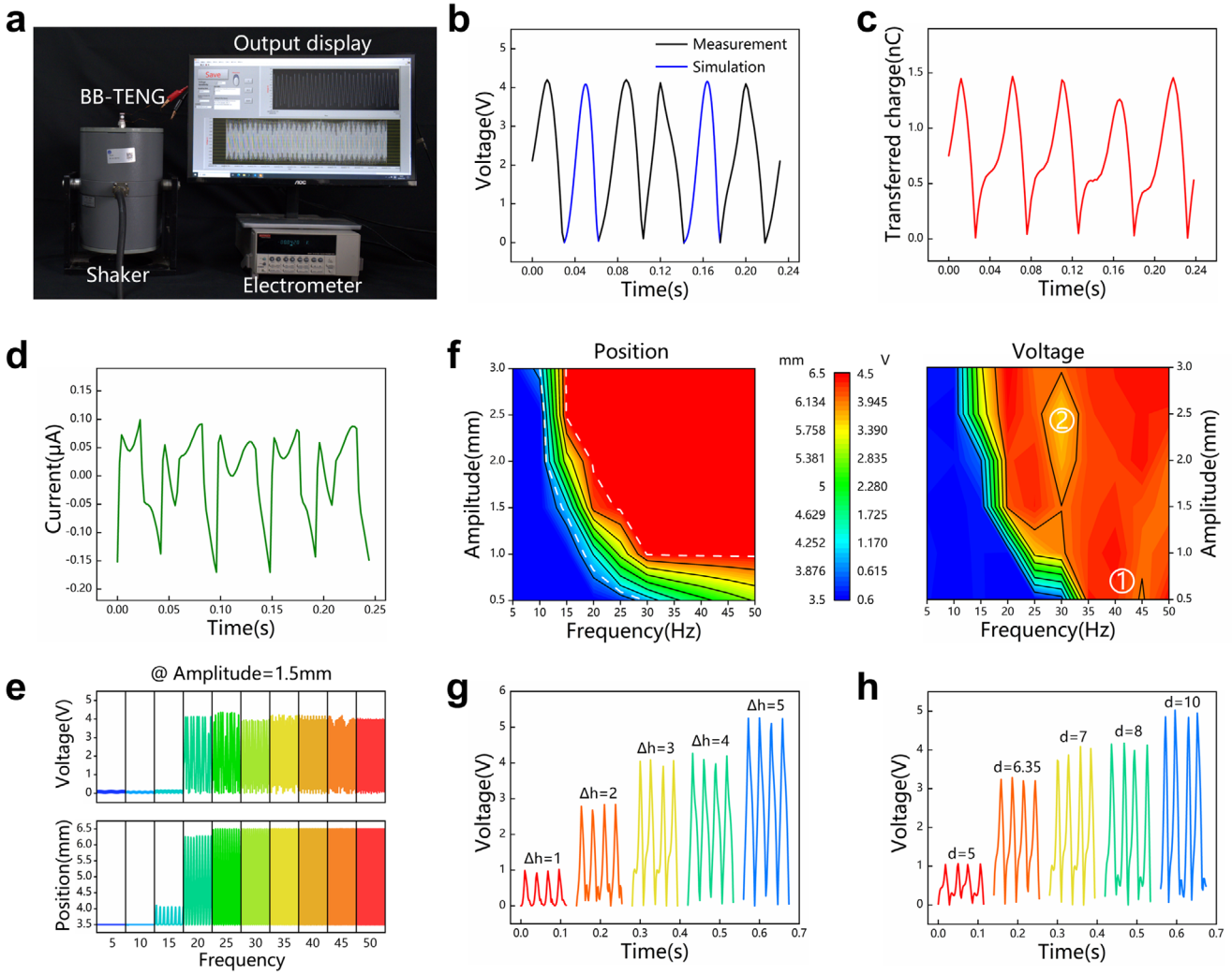

Figure 9. Electrical output performance of the BB-TENG. a) Photograph of the measurement setup. b) Comparison of the simulation and measurement results for voltage, c) transferred charge and (d) current of the vibration driven BB-TENG. e) Measured voltage and simulated position at various vibration frequencies for a fixed amplitude of 1.5 mm. f) Comparison of position and voltage with different vibration frequencies and amplitudes. Measured voltages with (g) different spacings and (h) different diameters.

the triboelectric layers and the redistribution of all charges on the TENG. Based on this study, by using more detailed physical parameters and finer simulation step sizes for the BB-TENG system, the accuracy for the internal distance between the ball and plates (e.g., the dielectric layer and electrodes) at any given time instant t_n will be further improved, enabling more precise theoretical predictions. Traditionally, a theoretical model has been validated by comparing predicted voltage, current, and transferred charge with experimental data. In contrast, the method presents in this study integrates the multibody dynamic simulation and electrical finite element simulation. Specifically, the dynamic simulation provides the time-resolved motion trajectory of the bouncing ball. These outputs (such as Figure 8c) are then directly fed into the electrical finite element analysis as discrete inputs, allowing the direct computation of the electric signals, such as the voltage waveform in Figure 8d for quick performance prediction and model verification, eliminating the need of expensive and repetitive experiments. While this work focuses mainly on the vibration-driven freestanding-layer mode TENG, the proposed dual-simulation coupling method is also applicable to other mode TENGs,[51] providing a physically grounded and generalizable approach for performance prediction.

3.2. Electrical Output Characteristics of the BB-TENG

As described in Section 2.1, the electricity generated by the BB-TENG is measured by the electrometer, around which the test system is built up, as shown in **Figure 9**a. The copper electrodes of the tested BB-TENG are connected to the electrometer. The electrical signals are acquired by its data acquisition unit and then transferred to a computer-based LabVIEW program for display and storage. The measured V_{OC} under the same excitation as Figure 8c and the corresponding simulation result are integrated into Figure 9b for intuitive comparison. Since the simulated or actual contact almost occurs, the voltage at this time reaches the

maximum amplitude of 4.2 V achievable by the tested BB-TENG. The simulation agrees well with the experiment, whereas the errors mainly come from the input estimation errors. Specifically, the TENG material charge and the relative displacement jointly determine the peak, while the actual motion leads to the waveform. The magnitudes of Q_{SC} and I_{SC} measured using the electrometer of the BB-TENG are 1.42 nC and 0.16 μA, respectively, as shown in Figure 9c,d. Although V_{OC} and Q_{SC} correlate positively with $x(t)$, the shape of Q_{SC} differs. In the Metal-Dielectric-Metal mode, V_{OC} varies linearly with x, ensuring a relatively high slope in the whole range of x (as on the vertical axis of Figure 9(b)). But in Figure 9c, Q_{SC} exhibits a steep slope only at two ends, when x is in the middle as shown in Figure 8b(iii), it is nearly a constant. This phenomenon is consistent with the output characteristics reported by Niu et al.[43] As a comparison, the relative velocity v_r between the bouncing ball and its plates is simulated utilizing the same parameters and the results are plotted in Figure S8, Supporting Information. It can be seen that the basic waveform of I_{SC} is in phase with $v_r(t)$, confirming Equation (13). Similarly, from $I(t) = dQ/dt$, the lag in the transferred charge is also reflected in the wave peak of the current in Figure 9d.

The voltage signal with the superior linearity is chosen to further characterizing the output performance. Figure 9e presents the measured voltage of the BB-TENG and the simulated position of the bouncing ball for the vibration frequency ranging from 5 Hz to 50 Hz at a fixed amplitude of 1.5 mm. It can be seen that the variation trend of the peak-to-peak voltage matches closely the simulated results. As seen in Figure 4c, the ball in the experiment does not bounce at 15 Hz and 1.5 mm. Therefore, no electricity is generated in the BB-TENG when the vibration frequency is less than 16 Hz (as listed in Table S3, Supporting Information). Contact begins to occur at 20 Hz, leading to a dramatic increase in the bounce height and the voltage output. As expected, the voltages reach and maintain its maximum for the frequencies ranging from 20 Hz to 50 Hz. The absence of further increase in voltage can be explained by the following reasonable assumption. The motion of the bouncing ball can be simplified as sinusoidal $x(t) = A\sin(\omega t + \varphi)$and thus Equation (12) and (13) can be further expressed as

$$V_{OC}(t) = \frac{2\sigma x(t)}{\varepsilon_0} = \frac{2\sigma A\sin(\omega t + \varphi)}{\varepsilon_0} \tag{14}$$

$$I_{SC}(t) = \frac{2\sigma S v(t)}{d_0 + h - d} = -\frac{2\sigma S}{d_0 + h - d} 2\pi A f\cos(\omega t + \varphi) \tag{15}$$

The voltage depends solely on the position of the ball whereas the current is proportional to the frequency of the TENG. The measured currents, plotted in Figure S9, Supporting Information, show a strong linear relationship with frequency (with a correlation coefficient of 0.98). Increasing the excitation frequency can significantly enhance the current output of the TENG, consistent with results reported in previous studies.[21,34,51] Furthermore, the positions and the voltages over the full vibration range, obtained from both operating modes, are presented in Figure 9f and listed in Table S3, Supporting Information. They show a similar tendency, that is, (1) the electricity is generated once the ball begins to bounce, and (2) the output voltage of the BB-TENG reaches a plateau when the CoM position of the bouncing ball reaches 6.5 mm. The white truncation curves correspond to the critical conditions for the ball's bounce and contact discussed in Section 2.3. It can be seen that the peak value (> 4 V) saturates quickly after the ball bounces, showing a voltage output bandwidth exceeding 35 Hz under a vibration amplitude of 3 mm. As reported in previous studies,[7,52] the freestanding-layer mode TENGs already show advantages in broadband energy harvesting. In this study, the non-resonance nature of the bouncing ball and the non-autonomous of its system further expand the bandwidth.

It is worth noting that there are some fluctuations in the peak voltage appearing in the regions labeled 1 and 2. As analyzed in Section 2.3.2, chaos in the motion of the bouncing ball induced by low velocity at higher frequency, as Region 1 with the vibration amplitude of 0.5 mm and the frequencies from 35 Hz to 50 Hz, may cause mutations in the electrical output. Experimentally, we also found it difficult to adjust the shaker to maintain an amplitude of 0.5 mm at higher frequencies, which will introduce artificial errors. For Region 2, having hit the plate at a large relative velocity, the PTFE ball exhibits plasticity that confiscates most of the kinetic energy, while the elasticity leads the ball to perform some smaller bounces. This behavior corresponds to the sticking solutions shown from the simulation calculation in Figure 7. For the sake of visualization, see Video S4, Supporting Information at a vibration excitation of 30 Hz and 3 mm. As discussed in Section 2.3.2 and ref. [40] the sticking process that was supposed to happen will be destroyed by the collision duration when the impact velocity becomes small. Here, chaotic behaviors are also likely to be induced, thereby making the output fluctuate. Overall, the electrical output of the BB-TENG coincides with the dynamic response of the bouncing ball system.

Equally, the effects of the BB-TENG structural parameters, including the spacing Δh and the ball diameter d, on the output performance are analyzed.

(1) The effect of electrode spacing. Different middle tubes are replaced to form various spacings. The vibration condition of 35 Hz and 1.5 mm is selected, guaranteeing the bouncing balls can contact the upper electrode plates in the tubes of different heights, which is verified by the simulation displayed in Figure S6, Supporting Information. According to the measurement results in Figure 9g, the voltage shows a monotonously upward trend with Δh increases from 1 to 5 mm. In these sizes, the voltage output is still governed by Equation (12), and under sufficient excitation, the electrode spacing can be appropriately increased to improve the performance of the BB-TENG. Absolutely, this spacing cannot be increased without restriction. As shown in Figure S10, Supporting Information, the transferred charge achieves saturation at Δh = 3 mm, while the measured current drops off when Δh increases to 4 and 5 mm. The reason for the attenuation is as follows: The average velocity decreases with the prolongation of the rising and decelerating stage for the ball at the same initial velocity (as the same vibration excitation), and the current drops accordingly from Equation (13). Also, according to the parallel plate capacitor model $C = \varepsilon S/d$ followed by the TENG, excessive spacing will obviously destroy the interplate capacitance.

(2) The effect of ball diameter. PTFE balls in five common diameters of 5, 6.35, 7, 8, and 10 mm but corresponding fixed Δh = 3 mm are measured at 35 Hz and 1.5 mm. In Figure S7

(Supporting Information), all the bouncing balls can fully contact the upper electrode. Figure 9h gives the measured voltage of the BB-TENGs for different ball diameters *d*. Larger PTFE ball leads to more negative charges, by which more electrons are forced to flow in the external circuit. Therefore, macroscopically amplifying the overall sizes and connecting multiple units in parallel,[27,53] or microscopically strengthening the relative surface area by physical and chemical processes[54,55] are common methods to enhance the TENG performance. However, in practical application, it should also consider the obstruction from the TENG's mass and volume to the normal operation of the energy source.

3.3. Practical Applications of the Proposed Approach

Through high-speed camera verification and electrical performance test of the BB-TENG, the dynamic behaviors of the bouncing ball predicted by the ADAMS simulation are found to be highly consistent with the actual motion and the measured output results. This consistency also indicates the proposed dual-coupled simulation method is promising for analyzing the characteristics of the TENGs and optimizing their design, especially in cases where the basic parameters have not yet been finalized.

BB-TENG based energy harvesters and self-powered sensors have attracted attention across various fields due to their unique characteristics.[7] In our recent study,[13] a self-powered ammonia leakage monitoring device designed for zero-carbon emission ships has been demonstrated. For this application, the BB-TENG structure needs to be customized according to the actual vibration condition, a process guided and validated by the proposed approach. The monitoring device is mounted on the diesel generator of a real ship named M.V. "YU KUN" to detect the ammonia leakage in the engine room. The dominant working frequency of this diesel engine with the type of WÄRTSILÄ Auxpac 520W4L20 is ≈33 Hz (details are shown in Experimental Section), and the measured vibration amplitudes at several possible installation positions are found to range from 0.5 to 1 mm. To minimize weight and volume, the PTFE balls with a smallest diameter of 5 mm are selected. Assuming a median vibration amplitude of (0.5 + 1)/2 = 0.75 mm, the ADAMS simulation predicts a stable jumping height of over 2 mm but not up to 3 or 2.5 mm at 33 Hz, as confirmed in Figure S11, Supporting Information. Consequently, the height of the BB-TENG middle container *h* is set to be 7 mm to ensure regular and full contact with a larger stroke ($\Delta h = 2$ mm).

The electric power produced by a single BB-TENG is limited, integrating multiple units is inevitable. As schemed in **Figure 10a**, five layers of honeycomb-structured containers are designed and connected in parallel, ensuring sufficient power output while minimizing the occupied space. Each layer contains 91 PTFE balls. The honeycomb containers and the end plates are made of polylactic acid (PLA) and fabricated by 3D printing technology. The regular hexagon geometry of the honeycomb is the most efficient topology of covering a 2D plane,[12,56] which not only allows for more BB-TENG cells (as the red shadow) to be accommodated within the same area, but also requires the least material consumption for 3D printing and provides a significant strength. A flexible ultrathin sponge is inserted between the copper electrode and the PLA plate to increase the contact area and stabilize the dynamic behavior of the bouncing ball. As shown in Figure 10b, the honeycomb TENG achieves peak values of V_{OC}, Q_{SC} and I_{SC} of 342.56 V, 153.14 nC and 26.72 μA. It can be observed from Figure S12, Supporting Information that all electrical outputs increase approximately linearly with the number of balls. Figure S13, Supporting Information shows the instantaneous power density of the honeycomb TENG by applying different external load resistances, with a maximum of 59.78 W m^{-3} obtained at 11 MΩ, which is sufficient meet the power requirements of the entire detection system. In operation, the TENG harvests vibration energy and converts it into electrical power. Then, the LTC3588 integrated circuit transforms the instantaneous current into a constant voltage output for the detecting system. The detailed experimental process and results can be found in ref. [13]. When NH_3 molecules adsorb onto the carbon nanotube doped polypyrrole (CNTs-PPy) surface, electrons transfer from the NH_3 molecules to the CNTs-PPy, neutralizing the holes in the material. This reduces the charge carrier concentration in CNTs-PPy, resulting in an increase in sensor resistance and thereby producing a measurable voltage variation across the fixed load.

Finally, a series of experiments are conducted on M.V. "YU KUN" to test the performance of the system in real scenarios. Figure 10c displays the photography of the honeycomb TENG mounted on the test diesel engine. And the designed TENG maintains high performance over extended periods during continuous engine operation, as shown in Figure 10d. The complete self-powered detection device is then tested in the presence of NH_3 gas in the engine room. As the ammonia concentration increases, the voltage across the load decreases gradually with a short response time. Subsequently, the signal returns to its original level once the gas dissipate. Overall, the honeycomb TENG has demonstrated excellent practicality and reliability in this applied study.

4. Conclusion

This study systematically analyzes the BB-TENG through integrated dynamic simulations and electrical measurements. The non-uniform dielectric motion forms the physical foundation of energy conversion in TENGs. Referring to a vibration-driven bouncing ball system with limiters, key parameters including vibration intensity, restitution coefficient, distance between two plates, and ball diameter are comprehensively analyzed. Bounce, chaos, critical contact, and regular contact, four typical motion states are revealed using ADAMS dynamic simulations. Among them, bounce initiates electricity generation, regular contact produces the maximum stable output, and chaos leads to a fluctuating output. These behaviors are experimentally verified using a high-speed imaging system and synchronized electrical measurements, confirming the superior linearity of the electromechanical response in freestanding-layer mode TENGs. Meanwhile, the motion trajectories derived from simulations are further coupled into COMSOL finite element models to calculate electric potentials, enabling rapid performance prediction and model validation without repetitive experiments. This combined analysis method is effective for future design and optimization of the BB-TENG can be extended to other TENG modes. Finally, a case demonstration on a multilayer honeycomb BB-TENG

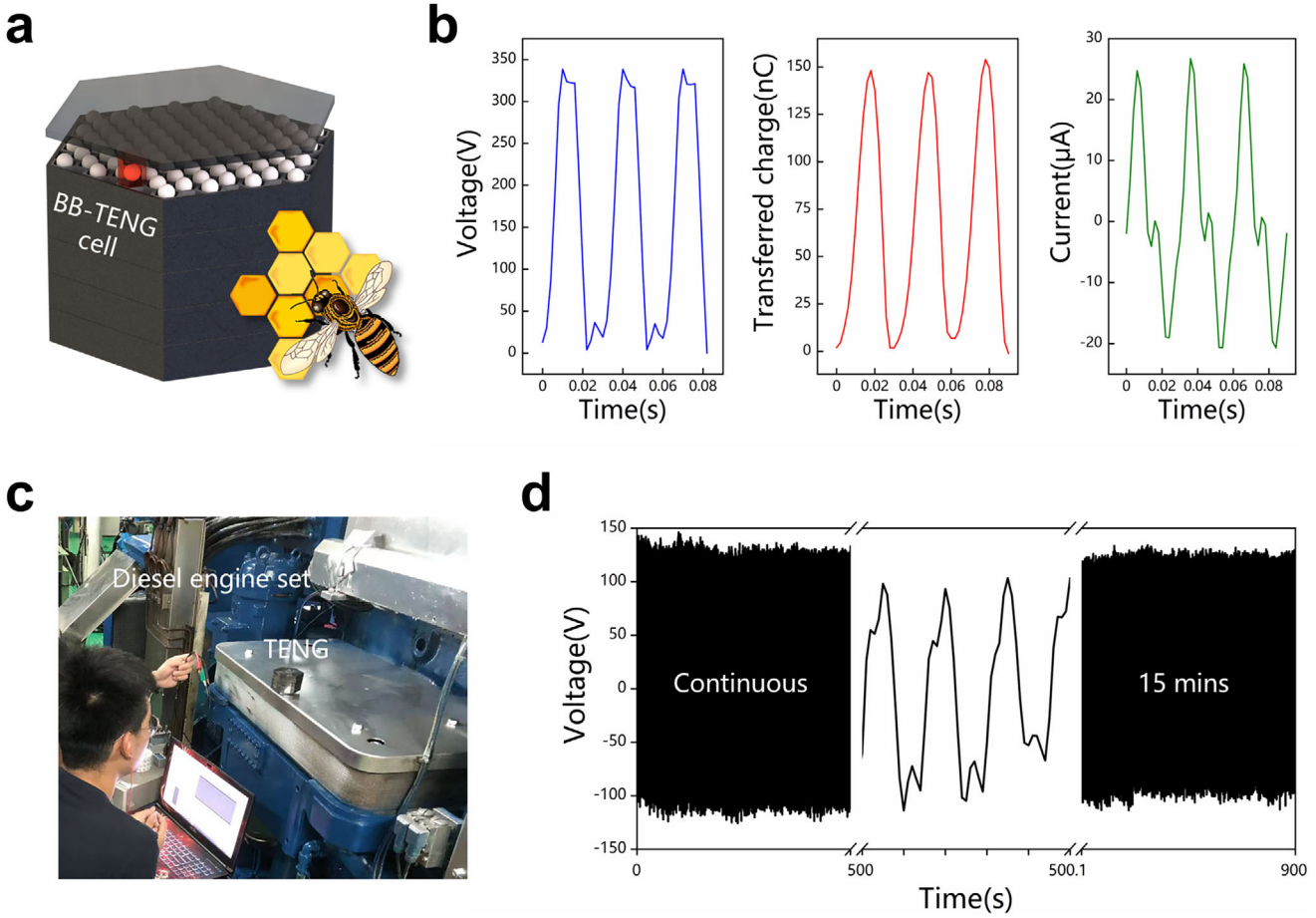

Figure 10. Shipboard application of the BB-TENG. a) Honeycomb-inspired TENG comprising multiple BB-TENG cells. b) Voltage, transferred charge and current of the honeycomb TENG under simulated vibration excitation of 0.5 mm amplitude and 33 Hz frequency. c) Photograph of the honeycomb TENG installed on a marine diesel engine. d) Stable output performance over 15 min.

powering an ammonia sensor aboard a real ship verifies the feasibility of this method. The proposed multidimensional dynamic analysis and coupled simulations enable the precise design and optimization of TENG structures, and advance the standardization and practicality of triboelectric technology.

5. Experimental Section

Fabrication of the BB-TENG and Measurement Process: The tested BB-TENG consists of an acrylic cylindrical tube, a PTFE ball, and two copper electrodes stuck on the acrylic circular plates with back glue. The electrode layer is the copper foil tape with a thickness of 1 mm. Two copper wires were adhered to the copper electrodes as the electrical output wires, respectively. The acrylic tube has an inner diameter of 8 mm, an outer diameter of 11 mm and a height of 10 mm, forming the BB-TENG container with two parallel acrylic plates that have a diameter of 11 mm and a thickness of 2 mm. The PTFE ball with a diameter of 7 mm was placed in the container as the free layer. All TENG units and their accessories were fabricated in a dry room temperature environment to minimize the impact of external moisture. The assembled BB-TENG was mounted on the table of an electromagnetic shaker (JZK-10), which is driven by an amplified sinusoidal signal from a function generator (YE1311) and a charge amplifier (YE5852). A high-speed camera (Phantom V2012) operated at 2000 fps was used to capture the motion of the ball with sufficient sampling accuracy. Electric output signals, including open-circuit voltage, short-circuit current and transferred charges, were measured and acquired by a Keithley 6514 electrometer and an NI 9215 analog-to-digital converter. The data was sent to the LabView software based on the computer with a sampling frequency of 500 Hz. The subsequent calculations and plots are carried out in the MATLAB and Origin software.

Simulation Methods: All models were built according to the actual dimensions of the tested BB-TENG. For dynamic simulation via the ADAMS software (Adams View 2020), the 3D component models were first established and assembled, where the copper electrodes were excluded reasonably considering its thin thickness. The upper plate, the lower plate and the middle tube were connected by Boolean operation to provide a closed space for the bouncing ball. After the prototype was created, the corresponding materials and physical properties were assigned separately. Then, motion pairs, drives, and contacts were applied to the components using the ADAMS library. The assembled container was driven by a translation pair, and the driver function in ADAMS is expressed as $y = A \times \sin(2 \times pi \times f \times time)$. Force contact with a type of entity-to-entity was introduced between the bouncing ball and the upper plate, the bottom plate and the middle tube, respectively. Coulomb friction was activated, with static and dynamic friction coefficients set to 0.1 and 0.05, respectively. To track the motion of the bouncing ball, a point-to-point measurement was added between the CoM of the bouncing ball and the center of the lower plate surface.

A 2D model were established in the COMSOL software (COMSOL Multiphysics 5.6), using AD/DC module with a static electric field and steady-state analysis. A large air space was created, and all edges of the air domain were set as infinite element domains to ensure that the electric field distribution from the TENG is least affected by the spatial boundaries. The applicable values of the parameters including dielectric permittivity, thickness and charge density were entered for each simulation area. In open-circuit conditions, the outer surface of the PTFE ball was assigned a surface charge density of 8×10^{-6} C m^{-2},[50] while the two planar electrodes were both assigned the corresponding suspension potential and grounding. The continuous simulation signal of the ball is calculated by interpolation and parametric scanning based on the simulated motion trajectory.

On-Board Vibration Test: The on-board test was carried out while the M.V. "YU KUN" was mooring in Dalian Port, with the diesel generator operating under normal conditions. Generally, structural vibration of diesel engines originates from the change of gas pressure during the combustion process in the cylinder. The WÄRTSILÄ Auxpac 520W4L20 diesel generator served in "YU KUN" is equipped with four cylinders and rates at 1000 rpm. Each cylinder works 1000/2 = 500 combustion cycles per minute. Therefore, the diesel engine works 2000 times per minute, resulting in a theoretical vibration frequency of ≈2000/60 ≈ 33.33 Hz.

Supporting Information

Supporting Information is available from the Wiley Online Library or from the author.

Acknowledgements

The work was supported by the National Natural Science Foundation of China (Grant No. 52371345), and the China Postdoctoral Science Foundation (Grant Nos. 2025T180074 and 2024M750297).

Conflict of Interest

The authors declare no conflict of interest.

Data Availability Statement

The data that support the findings of this study are available from the corresponding author upon reasonable request.

Keywords

bouncing ball systems, dynamic behavior, triboelectric nanogenerators, vibration energy harvesting

Received: September 17, 2025
Revised: November 4, 2025
Published online:

[1] J. F. M. Oudenhoven, R. J. M. Vullers, R. Schaijk, *Int. J. Energy Res.* **2012**, *36*, 1139.
[2] Y. Zhang, W. Wang, X. Wu, Y. G. Lei, J. Y. Cao, C. Bowen, S. Bader, B. Yang, *Renewable Sustainable Energy Rev.* **2023**, *183*, 113446.
[3] A. Mohammadnia, A. Rezania, B. M. Ziapour, F. Sedaghati, L. Rosendahl, *Energy Convers. Manage.* **2020**, *205*, 112352.
[4] O. H. Ando, A. L. O. Maran, N. C. Henao, *Renewable Sustainable Energy Rev.* **2018**, *91*, 376.
[5] X. Q. Ma, S. X. Zhou, *Energy Convers. Manage.* **2022**, *254*, 115223.
[6] H. Cai, T. L. Du, F. Y. Dong, Z. X. Chen, D. L. Shen, Y. J. Zou, M. Y. Xu, *Nano Energy* **2024**, *132*, 110363.
[7] T. L. Du, F. Y. Dong, Z. Y. Xi, M. X. Zhu, Y. J. Zou, P. T. Sun, M. Y. Xu, *Small* **2023**, *19*, 27.
[8] F. U. Khan, *J. Renewable Sustainable Energy* **2016**, *8*, 38.
[9] D. L. Shen, T. L. Du, F. Y. Dong, H. Cai, A. Noor, X. N. Du, Y. J. Zou, C. Lee, M. Y. Xu, *Int. J. Extreme Manuf.* **2025**, *7*, 33.
[10] M. Iqbal, M. M. Nauman, F. U. Khan, P. E. Abas, Q. Cheok, A. Iqbal, B. Aissa, *Int. J. Energy Res.* **2021**, *45*, 65.
[11] Z. P. Cai, Q. Chen, T. Shi, T. X. Zhu, K. Y. Chen, Y. S. Li, *IEEE Internet Things J.* **2023**, *10*, 5543.
[12] X. Xiao, X. Q. Zhang, S. Y. Wang, H. Ouyang, P. F. Chen, L. G. Song, H. C. Yuan, Y. L. Ji, P. H. Wang, Z. Li, M. Y. Xu, Z. L. Wang, *Adv. Energy Mater.* **2019**, *9*, 11.
[13] J. Y. Chang, C. Q. Zhu, Z. M. Wang, Y. Wang, C. S. Li, Q. Hu, R. J. Xu, T. L. Du, M. Y. Xu, L. Feng, *Nano Energy* **2022**, *98*, 107271.
[14] R. Guo, K. Zhuo, X. J. Cui, W. D. Zhang, S. B. Sang, H. L. Zhang, *Energy Technol.* **2020**, *8*, 6.
[15] P. F. Ji, J. Wen, X. B. Gao, H. Li, H. S. Cai, K. Lv, Z. L. Wang, B. D. Chen, R. harvester, *Sci. Adv.* **2025**, *11*, 13.
[16] L. F. Zhu, Z. C. Zhang, D. J. Kong, C. B. Liu, Z. G. Cao, W. Q. Chen, C. L. Zhang, *Nano Energy* **2022**, *97*, 107165.
[17] Z. Liu, Y. R. Hu, X. C. Qu, Y. Liu, S. J. Cheng, Z. M. Zhang, Y. Z. Shan, R. Z. Luo, S. X. Weng, H. Li, H. X. Niu, M. Gu, Y. Yao, B. J. Shi, N. N. Wang, W. Hua, Z. Li, Z. L. Wang, *Nat. Commun.* **2024**, *15*, 11.
[18] S. Saadon, O. Sidek, *Energy Convers. Manage.* **2011**, *52*, 500.
[19] A. Muscat, S. Bhattacharya, Y. Zhu, *Sensors* **2022**, *22*, 5555.
[20] X. H. Zhang, J. Q. Zhao, X. P. Fu, Y. Lin, Y. C. Qi, H. Zhou, C. Zhang, *Nano Energy* **2022**, *98*, 107209.
[21] T. L. Du, X. S. Zuo, F. Y. Dong, S. Q. Li, A. E. Mtui, Y. J. Zou, P. Zhang, J. H. Zhao, Y. W. Zhang, P. T. Sun, M. Y. Xu, *Micromachines* **2021**, *12*, 14.
[22] G. B. Li, Q. T. Li, W. H. Hao, J. Li, H. Z. Guo, X. Q. Zheng, C. M. Huang, *Nano Energy* **2022**, *104*, 107864.
[23] K. K. Wang, Y. X. Liu, X. Guan, Z. H. Wang, Z. P. Pan, Y. Yu, Y. M. Yao, T. Y. Li, *IEEE Trans. Ind. Electron.* **2025**, *72*, 11964, https://doi.org/10.1109/tie.2025.356185411.
[24] J. Cui, X. Li, K. P. Wang, X. L. Yan, Y. Q. Zheng, C. Y. Xue, *Nano Energy* **2025**, *133*, 110481.
[25] L. N. Y. Cao, E. R. Su, Z. J. Xu, Z. L. Wang, *Mater. Today* **2023**, *71*, 9.
[26] Y. Wang, T. Y. Chen, S. W. Sun, X. Y. Liu, Z. Y. Hu, Z. H. Lian, L. Liu, Q. F. Shi, H. Wang, J. C. Mi, T. M. Zhou, C. K. Lee, M. Y. Xu, *Nano Res.* **2022**, *15*, 3246.
[27] Y. W. Wang, H. X. Du, H. Y. Yang, Z. Y. Xi, C. Zhao, Z. Qian, X. Chuai, X. Z. Peng, H. Y. Yu, Y. Zhang, X. Li, G. B. Hu, H. Wang, M. Y. Xu, *Nat. Commun.* **2024**, *15*, 11.
[28] C. Q. Zhu, M. W. Wu, C. Liu, C. Xiang, R. J. Xu, H. Y. Yang, Z. Y. Wang, Z. Y. Wang, P. Xu, F. Z. Xing, H. Wang, M. Y. Xu, *Adv. Energy Mater.* **2023**, *13*, 11.
[29] H. Wang, Z. Q. Fan, T. C. Zhao, J. L. Dong, S. Y. Wang, Y. Wang, X. Xiao, C. X. Liu, X. X. Pan, Y. P. Zhao, M. Y. Xu, *Nano Energy* **2021**, *84*, 105920.
[30] H. Wang, C. Q. Zhu, W. C. Wang, R. J. Xu, P. F. Chen, T. L. Du, T. X. Xue, Z. Y. Wang, M. Y. Xu, *Nanomaterials* **2022**, *12*, 12.
[31] R. N. Li, X. L. Wei, J. H. Xu, J. H. Chen, B. Li, Z. Y. Wu, Z. L. Wang, *Micromachines* **2021**, *12*, 10.
[32] C. Wu, H. Huang, R. Li, C. X. Fan, *Sensors* **2020**, *20*, 11.
[33] F. R. Fan, Z. Q. Tian, Z. L. Wang, *Nano Energy* **2012**, *1*, 328.
[34] H. F. Zhao, H. Wang, H. Y. Yu, Q. H. Xu, X. S. Li, J. Guo, J. J. Shao, Z. L. Wang, M. Y. Xu, W. B. Ding, *Energy Environ. Sci.* **2024**, *17*, 2228.
[35] R. H. Li, R. Y. Qiu, Y. H. Zhou, *Int. J. Non-Linear Mech.* **2018**, *105*, 268.

[36] M. Lampart, J. Zapomel, *Math. Meth. Appl. Sci.* **2016**, *39*, 4923.
[37] J. J. Barroso, M. V. Carneiro, E. E. N. Macau, *Phys. Rev. E* **2009**, *79*, 10.
[38] Z. H. Lai, G. Thomson, D. Yurchenko, D. V. Val, E. Rodgers, *Mech. Syst. Signal Proc.* **2018**, *107*, 105.
[39] R. H. Li, R. Y. Qiu, *Mod. Phys. Lett. B* **2021**, *35*, 25.
[40] Z. H. Jiang, Z. J. Liang, A. C. Wu, R. H. Zheng, *Physica A* **2018**, *494*, 380.
[41] H. H. Ruan, T. X. Yu, *Int. J. Impact Eng.* **2016**, *88*, 1.
[42] Z. L. Wang, *Mater. Today* **2017**, *20*, 74.
[43] S. M. Niu, Y. Liu, X. Y. Chen, S. H. Wang, Y. S. Zhou, L. Lin, Y. N. Xie, Z. L. Wang, *Nano Energy* **2015**, *12*, 760.
[44] T. X. Yu, *Mechan. Eng.* **2022**, *44*, 918.
[45] Z. J. Kowalik, M. Franaszek, P. Pieranski, *Phys. Rev. A* **1988**, *37*, 4016.
[46] M. Luck, *Phys. Rev. E: Stat. Phys., Plasmas Fluids Relat. Interdiscip. Top.* **1993**, *48*, 3988.
[47] C. Xu, Y. L. Zi, A. C. Wang, H. Y. Zou, Y. J. Dai, X. He, P. H. Wang, Y. C. Wang, P. Z. Feng, D. W. Li, Z. L. Wang, *Adv. Mater.* **2018**, *30*, 9.
[48] H. Y. Zou, Y. Zhang, L. T. Guo, P. H. Wang, X. He, G. Z. Dai, H. W. Zheng, C. Y. Chen, A. C. Wang, C. Xu, Z. L. Wang, *Nat. Commun.* **2019**, *10*, 9.
[49] X. Guo, J. Shao, M. Willatzen, X. Wang, Z. L. Wang, *Adv. Phys. Res.* **2023**, *2*, 2200039.
[50] X. S. Meng, H. Y. Li, G. Zhu, Z. L. Wang, *Nano Energy* **2015**, *12*, 606.
[51] F. Y. Dong, M. X. Zhu, Y. L. Wang, Z. X. Chen, Y. W. Dai, Z. Y. Xi, T. L. Du, M. Y. Xu, *Nano Energy* **2025**, *134*, 110550.
[52] T. L. Du, D. L. Shen, Z. Y. Xi, H. Y. Yu, F. Y. Dong, C. Zhao, M. X. Zhu, Y. J. Zou, P. T. Sun, M. Y. Xu, *Nano Res.* **2024**, *17*, 4089.
[53] Y. Yu, H. Y. Li, X. S. Zhang, Q. Gao, B. R. Yang, Z. L. Wang, T. H. Cheng, *Joule* **2024**, *8*, 1855.
[54] J. Wang, C. S. Wu, Y. J. Dai, Z. H. Zhao, A. Wang, T. J. Zhang, Z. L. Wang, *Nat. Commun.* **2017**, *8*, 8.
[55] S. H. Wang, Y. L. Zi, Y. S. Zhou, S. M. Li, F. R. Fan, L. Lin, Z. L. Wang, *J. Mater. Chem. A* **2016**, *4*, 3728.
[56] T. C. Hales, *Discret. Comput. Geom.* **2001**, *25*, 1.